

Article

A Self-Growing 3D Porous Sn Protective Layer Enhanced Zn Anode

Dezhi Kong¹, Qingwei Zhang¹, Lin Li², Huimin Zhao¹, Ruixin Liu¹, Ziyang Guo^{1,*} and Lei Wang^{1,3,*}

¹ Key Laboratory of Eco-Chemical Engineering, Taishan Scholar Advantage and Characteristic Discipline Team of Eco-Chemical Process and Technology, College of Chemistry and Molecular Engineering, Qingdao University of Science and Technology, Qingdao 266042, China

² School of Materials Science and Engineering, Suzhou University of Science and Technology, Suzhou 215009, China

³ College of Environment and Safety Engineering, Qingdao University of Science and Technology, Qingdao 266042, China

* Correspondence: zyguo@qust.edu.cn (Z.G.); inorchemwl@qust.edu.cn (L.W.); Tel./Fax: +86-0532-8402-3409 (L.W.)

Abstract: Aqueous zinc-ion batteries (ZIBs) have received much attention because of their high safety, low pollution, and satisfactory energy density (840 mAh g^{-1}), which is important for the research of new energy storage devices. However, problems such as short cell cycle life and low coulombic efficiency (CE) of zinc (Zn) anodes due to disorderly growth of Zn dendrites and side reactions of hydrogen corrosion have delayed the practical application of ZIBs. In this work, a new “self-growth” method is proposed to build a robust and homogeneous three-dimensional (3D) nanoporous structure of tin (Sn)-coated Zn anodes (ZSN) in just 10 min by a simple and fast reaction, which can largely raise the surface area of the electrode plate. The ZSN not only provides abundant Zn nucleation sites, but also reduces the corrosion current, thus alleviating the self-corrosion of the electrolyte, reducing the occurrence of hydrogen precipitation side reactions, and effectively inhibiting the growth of Zn dendrites during cycling. Thus, a symmetric cell with a ZSN anode can be stabilized with very low voltage hysteresis (30 mV) for 480 h of stable plating/stripping cycles and can operate well for 200 h even at high current densities of 10 mA cm^{-2} . Supercapacitors and button cells were assembled, respectively, to verify the performance of ZSN electrodes in different energy storage tools. The ZSN || AC supercapacitor exhibited superior capacity (75 mAh g^{-1}) and high reversibility (98% coulombic efficiency) at a current density of 2 A g^{-1} . With a MnVO (MVO) electrode as the cathode, the ZSN || MVO full cell presents excellent cycling stability with a capacity retention of 95.4% after 500 cycles at 2 A g^{-1} , which far exceeds that of the bare Zn cell.

Keywords: nanoporous anode; aqueous Zn-based battery; dendrite-free; 3D metal versatile protective layer



Citation: Kong, D.; Zhang, Q.; Li, L.; Zhao, H.; Liu, R.; Guo, Z.; Wang, L. A Self-Growing 3D Porous Sn Protective Layer Enhanced Zn Anode. *Batteries* **2023**, *9*, 262. <https://doi.org/10.3390/batteries9050262>

Academic Editor: Guanjie He

Received: 23 February 2023

Revised: 24 April 2023

Accepted: 28 April 2023

Published: 6 May 2023



Copyright: © 2023 by the authors. Licensee MDPI, Basel, Switzerland. This article is an open access article distributed under the terms and conditions of the Creative Commons Attribution (CC BY) license (<https://creativecommons.org/licenses/by/4.0/>).

1. Introduction

Widespread reliance on fossil fuels and growing energy demand are driving the development of new and sustainable energy technologies. Rechargeable metal batteries are expected to store renewable energies such as wind, solar, and tidal energies on a large scale [1–4]. Among these, lithium-ion batteries (LIBs) have been widely used due to their excellent electrical properties [5,6]. However, LIBs are still suffering from high battery costs and poor safety and are not suitable for high-current charging and discharging of existing power tools [7–9]. Recently, aqueous zinc-ion batteries (ZIBs) have emerged as one of the most attractive candidates for rechargeable metal-ion batteries [10,11]. Firstly, Zn metal is abundant and environmentally friendly, which is conducive to low-cost and large-scale applications. Secondly, the high volumetric capacity (5855 mAh cm^{-3}), the theoretical specific capacity (820 mAh g^{-1}), and the low redox potential contribute to the realization

of high-energy cells [12–14]. Thirdly, aqueous electrolytes, especially ZnSO_4 electrolytes, which have been extensively studied in recent years, are inherently safe and compatible with Zn metal anodes to ensure the safety of ZIBs [15–18]. Research on ZIBs has focused on the development of cathode materials and energy storage mechanisms, whereas attention to the anodes is insufficient [19–21]. For the moment, Zn metal anodes are still suffering from uneven electrochemical coatings and unavoidable corrosion side reactions [22]. Additionally, the formation of Zn dendrites with an ultra-high Young's modulus (108 GPa) can puncture the celgard separator and cause short circuits that result in battery failure, which consequently prevents the eventual commercial application of rechargeable aqueous Zn batteries [23]. Therefore, constructing stable and rechargeable Zn anodes is of considerable importance for high-performance ZIBs [24]. So far, various strategies have been proposed to solve these problems [25], including interfacial modification, structural design, novel electrolyte additives, and diaphragm modification [26–30]. Electrolyte additives can harmonize the electrolyte environment, homogenize the interfacial electric field, and induce Zn deposition [31]. For example, Liu et al. introduced a polyamino acid (PAA) as a multifunctional electrolyte additive to inhibit the growth of Zn dendrites on the Zn metal anode [32]. However, electrolyte additives are easily hydrolyzed and corrosive and present poor stability at high temperatures. Solid electrolytes can effectively avoid side reactions. Based on zirconium phosphate (ZrP), Yan et al. constructed a multifunctional artificial solid electrolyte interface on the Zn anode (Zn@ZrP) by a spraying method to achieve a high-stable dendrite-free Zn anode [33]. Nevertheless, unsatisfactory transport speeds and high fabrication costs for solid electrolytes need to be urgently solved. Although these strategies have improved the uniformity and reversibility of Zn deposition to some extent, the commercialization of rechargeable Zn metal batteries remains a challenge due to ongoing side reactions.

Interfacial modification techniques are receiving increasing attention due to their simplicity and structural versatility. The main objective of constructing artificial interfacial layers is to inhibit Zn dendrites, modulate the Zn^{2+} deposition behavior, and prevent direct contact between the Zn anode and the active water in the electrolyte, thus effectively mitigating the side reactions. It is worth noting that modulating the Zn^{2+} deposition behavior is an effective strategy to improve the reversibility and utilization of Zn anodes. A variety of materials have been used to prepare interfacial layers for high-performance Zn anodes, including carbon-based materials, metal-based materials, inorganic nonmetallic materials, polymers, and composites. Lu et al. constructed laminated double oxide (LDO) artificial interfacial protective coatings, which led to a more uniform plating/exfoliation process and improved corrosion resistance [34]. However, the oxide-modified coating still suffers from poor bonding to the electrode and easy deformation. Recently, metal coatings have been intensively investigated for their structural strength and high electrical conductivity. Cai et al. prepared a 3D forked-finger metallic Zn/solid electrolyte structure by an electrical substitution reaction between a metallic Zn foil and InCl_3 solution followed by electrochemical activation [35]. However, electrochemical activation is unable to form a robust and homogeneous 3D skeleton, which produces uncontrollable by-products. Immersion is a common method to fabricate 3D negative electrodes. Fan et al. made a unique 3D Zn alloy foam anode by immersing treated 3D porous Cu foam into a molten Zn-Sn-Pb alloy [36], which enhanced structural strength but unpleasantly raised the fabrication cost. In addition, the high temperature conditions required in the experiment increase the risk of the experiment [37–39].

Herein, we fabricated a unique “self-growing” metallic Sn coated on a Zn anode (ZSN) by a simple and rapid substitution reaction. The porous Sn coating layer provides fast ion transport and shows the high hydrogen evolution reaction (HER) overpotential to reduce the H_2O -induced side reactions and electrode volume variation. In addition, Sn, which possesses excellent zincophilicity, allows the surface electric field to be balanced, reducing the energy required for the Zn nucleation/deposition processes. Hence, the symmetrical cells assembled with ZSN electrodes display better performance than the bare Zn-based

symmetrical cells. Moreover, the ZSN||AC supercapacitors or ZSN||MVO full cells also show a long cycling life, good retention, or high coulombic efficiency. This simple and special anode construction method provides a new idea for the preparation of a new-type Zn metal battery and even other metal-based cells.

2. Experimental Section

2.1. Preparation of ZSN and ZS Electrodes

Zn foil was cut into square electrodes (1 mm × 1 mm) and immersed in dilute hydrochloric acid (12 vol%, analytical reagent, Aladdin Biochemical Technology Co., Ltd., Shanghai, China) for 5 min at room temperature to remove the surface oxidation passivation layer. The Zn foil was rinsed with ethanol (an analytical reagent, from Aladdin Biochemical Technology Co., Ltd., Shanghai, China) and set aside in an argon glove box. The Li foil was pressed onto the Zn foil using a hydraulic press and then sealed. The resultant composite foil was transferred to a beaker with 0.4 M SnCl₄ (an analytical reagent, Aladdin Biochemical Technology Co., Ltd., Shanghai, China) in ethanol for 10 min until the Li foil was completely dissolved. The ZSN electrode was washed after standing. Zn foil was reacted directly with SnCl₄ in ethanol following washing and drying to produce the ZS electrode.

2.2. Symmetric Cell Assembly

Symmetric cells were fabricated by pairing two ZSN electrodes or bare Zn electrodes in CR2032 coin cells. The thickness of the Zn foil used was 160 μm–170 μm. Glass fiber filters (GF/A, Whatman, Shanghai, China) were used as separators.

Unless otherwise specified, the battery electrolyte is 2 M ZnSO₄ electrolyte (weigh the corresponding mass of ZnSO₄·7H₂O particles and dissolve in deionized water). The volume of electrolyte is 100 μL and ensures wetting of the septum.

2.3. Assembly of the ZSN||AC Supercapacitor

The cathode slurry was prepared by mixing a commercial AC powder and PVDF in isopropanol at a weight ratio of 8:2 and then coated on carbon paper (cut as a circle with a diameter of 12 mm and a thickness of 10 μm, and an average mass of 9.1 mg), put into a vacuum drying oven, and dried at 60 °C for 12 h. The area mass loading of AC on the cathode electrode was about 1 mg cm⁻². The bare Zn, or ZSN, was used as the anode, and the AC electrode was applied as the cathode for the CR2032 button cell. A two-layer glass fiber filter (GF/A, Whatman Ltd., Shanghai, China) was used as the separator. The electrolyte (2 M ZnSO₄) was prepared by dissolving ZnSO₄ into deionized water. The electrolyte volume was fixed at 100 μL.

2.4. Synthesis of MnVO

A quantity of 0.74 g of V₂O₅ (Aladdin, >99.6%, Shanghai, China) was dissolved in 50 mL of distilled water, followed by the addition of 4 mL of H₂O₂ (Aladdin, 30%, Shanghai, China) dropwise using a pipette. This was followed by the preparation of another beaker weighing 0.34 g of MnSO₄·H₂O (Aladdin, ≥98%, Shanghai, China) dissolved in 60 mL of distilled water. Subsequently, the two solutions were poured into a 200 mL autoclave, placed in a vacuum drying oven, heated to 120 °C by setting a heating rate of 5 °C min⁻¹, and maintained at 120 °C for 10 h.

2.5. Assembly of ZSN||MVO Coin Cells

Pre-synthesized MnVO powder, acetylene black carbon, and PTFE in a total of 50 mg by weight in a ratio of 6:3:1 were mopped up in a mortar, and then 20 drops of isopropanol were added to prepare a slurry to be coated on Ti foil. After 12 h of drying, the foil was cut into circular pieces with a diameter of 12 mm (area mass loading of about 1.5 mg cm⁻²). The cathode was assembled in a CR2032 button cell with bare Zn or ZSN as the anode and an MVO electrode as the cathode. A two-layer glass fiber filter (GF/A, Whatman Ltd.,

Shanghai, China) was used as a separator. The electrolyte (2 M ZnSO₄) was prepared by dissolving ZnSO₄ into deionized water. The volume of the electrolyte was fixed at 100 μL.

3. Results and Discussion

A novel “self-growth” method is proposed to prepare ZSN electrodes. As shown in Figure 1a, the Li foil is driven thin by a simple physical pressure method and then pressed onto a Zn foil with a hydraulic press (5 Mpa). The pressure values can affect the mechanical properties of foils (Figure S1). Due to the external pressure, the smooth and soft metal Li foil is pressed tightly on the surface of the Zn foil. As a result, Zn and Li molecules at the contact area move irregularly and diffuse into each other’s molecular gaps, generating a special Zn-Li foil. The thickness of Zn-Li foil is 0.35 mm (Figure S2). In addition, the contact between metallic Zn and Li in the Zn-Li foil is very tight, and the surface of the Zn-Li foil is very flat (Figure S3). Then the Zn-Li foil is immersed in an ethanol solution of tin tetrachloride (SnCl₄), where the solvent ethanol can avoid the strong hydrolysis reaction of Sn. Li, as a highly reactive alkali metal, can react with ethanol following the equation: $2\text{Li} + 2\text{CH}_3\text{CH}_2\text{OH} = 2\text{CH}_3\text{CH}_2\text{OLi} + \text{H}_2\uparrow$. As a result, the detachment of Li from the Zn-Li foil will leave pores or microporous structures on the Zn surface. Meanwhile, a large amount of heat released by this reaction will favor the formation of 3D pores due to thermal expansion. When Li dissolves successively from the Zn-Li foil, the pores on the Zn surface originally occupied by Li change volume, and the accompanying atomic rearrangement apparently prevents passivation of the Zn foil surface and stops the production of other by-products. The unsaturated bonds in the remaining Zn are sufficiently reactive due to the detachment of the Li component to make the surface Zn much more reactive. Therefore, on the surface of Zn, SnCl₄ undergoes substitution reactions with Zn ($\text{Zn} + \text{SnCl}_4 = \text{SnCl}_2 + \text{ZnCl}_2$, $\text{Zn} + \text{SnCl}_2 = \text{Sn} + \text{ZnCl}_2$). The zincophilic nature of the metallic Sn nanoparticles is excellent. Ultimately, a porous Zn foil after detaching Li is uniformly covered with a three-dimensional porous Sn metal layer on the surface. The “self-growing” preparation method of ZSN electrodes does not require the pre-preparation of complex matrix skeletons and subsequent electrochemical activation, providing a research direction for new 3D composite anodes.

The morphology of ZSN electrodes was explored by SEM (Scanning Electronic Microscopy) testing. Visible scratches and rough surfaces can be clearly observed on the bare Zn electrode, (Figure 1b), while the ZS electrode was covered by an uneven milky white Sn layer with a partially fractured surface (Figure S4). The Sn layer shrank due to associated strain from the volatilization of ethanol molecules, which led to the cracking of the soft part of the Sn layer. In contrast to the ZS electrode, the surface of the ZSN electrode was covered by a 3D porous metal-tin coating with a pore size of about 1 μm (Figure 1c,d) without any crack on the surface. The hard 3D porous structure was sufficient to cope with the stress and surface tension derived from ethanol, which demonstrated the robustness of the metal-Sn coating as a protective layer. The cross-sectional image of the ZSN electrode shows that the thickness of the metallic Sn layer was about 30 μm (Figure 1e). The elemental composition of the protective layer is explored by energy dispersive X-ray spectroscopy (EDX) analysis. The result indicated that Zn, O, and Sn elements were uniformly distributed on the electrode surface (Figure 1f). A clear layered Sn structure is observed in the cross-sectional EDS elemental profile of the ZSN electrode (Figure S5), and the introduction of the bottom Sn element may be due to the occurrence of a common substitution reaction similar to that on the surface of the ZSN electrode. The composition of the ZSN electrode was further examined by X-ray diffraction (XRD). The characteristic peaks of 31, 32, 45, and 63° in Figure 1g could be clearly identified for the presence of Sn (04-0673), which manifested the main component of the surface coating as Sn. Additionally, the presence of Sn assisted in retarding the corrosion of the Zn anode and the HER in the electrochemical reaction. The characteristic peaks of Zn at 36, 39, 43, 54, 70, 70.5, 82, and 86° (Figure 1g) were consistent with the spectrum of a bare Zn electrode (Figure S6). In addition, X-ray photoelectron spectroscopy (XPS) tests were performed to further verify

the elemental species in ZSN (Figure 1h), and high-resolution XPS spectra of Zn 2p_{3/2} and Zn 2p_{1/2} were detected at 1021.9 and 1044.8 eV. Between Zn 2p_{3/2} and Zn 2p_{1/2}, the splitting energy of 23 eV represents a typical binding energy of Zn²⁺ (Figure 1i), indicating that Zn is involved in the substitution reaction at the electrode surface. Therefore, the ZSN electrode was mainly composed of Zn and Sn. As shown in Figure 1j, the peak at 485.0 eV was a typical monomeric Sn 3d peak, while the peaks at 497.0 and 494.0 eV were probably ascribed to SnO and SnO₂ (the oxidation products in air), respectively. In conclusion, all the above characterizations confirmed the formation of 3D porous Sn layer-protected composite electrodes.

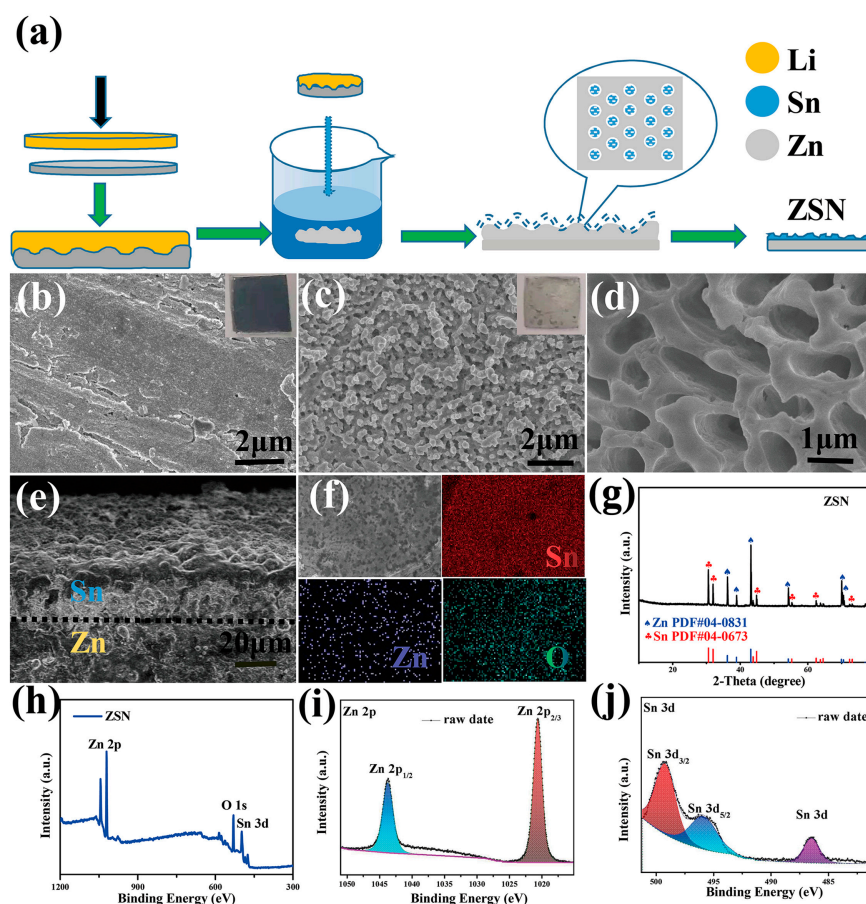


Figure 1. Preparation and characterization of bare Zn and ZSN electrodes. (a) Schematic diagram of the preparation process of the ZSN electrode. SEM images of (b) bare Zn and (c) ZSN electrodes (the inset shows actual optical photos of ZSN and bare Zn electrodes). (d) High-resolution and (e) cross-sectional images of the ZSN electrode. (f) Elemental mapping images of Sn, Zn, and O of the ZSN electrode. (g) X-ray diffraction pattern of the ZSN electrode. (h–j) High-resolution XPS spectra of ZSN (h), Zn 2p (i), and Sn 3d (j).

The influence of the Sn⁴⁺ concentration (0.2 M, 0.4 M, and 0.6 M) during the reaction on the electrochemical performance of the ZSN anode was explored at a current density of 0.5 mA cm⁻² for 0.5 mAh cm⁻² (Figure S7). The symmetrical cells assembled with the ZSN anode treated with 0.4 M Sn⁴⁺ exhibited the smallest overpotential (20 mV) and the longest cycle life. Therefore, the ZSN anode treated with 0.4 M Sn⁴⁺ was selected for the following work, unless otherwise noted. To explore the influences of the porosity and Sn on the performance of the Zn anodes, the controlled cycling experiment was performed with just porous Zn without Sn (ZL) and ZnSn without porosity (ZS) (Figure S8). The charge-discharge curves of the ZL or ZS based symmetrical cells fluctuate very badly at 1 mA cm⁻² for 1 mAh cm⁻². In contrast, the ZSN symmetrical cell showed good cycling stability over

a period of up to 450 h. The stability of the ZSN anode was evaluated by studying the long-term constant current cycling for assembled ZSN||ZSN and Zn||Zn symmetric cells at various current densities and specific capacities (Figure 2a–c). At 1 mA cm^{-2} (1 mAh cm^{-2}), the average overpotential of the Zn metal electrode was 140 mV for the first 70 cycles, but the polarization voltage of the bare Zn symmetric cells suddenly dropped after 70 cycles (Figure 2a) because the growth of a large number of dendrites penetrated the diaphragm, which resulted in a short-circuit. In contrast, the ZSN symmetric cells exhibited good cycling stability over a period of up to 460 h (Figure 2a). Notably, the overpotential value of the ZSN cell (20 mV) is much lower than that of the bare Zn symmetric cell (140 mV), which was superior to those for many recently reported anode matrixes (Table S1). The unique 3D porous Sn structure can guide Zn^{2+} nucleation at specific locations and prevent the generation of sharp dendrites at 2 mA cm^{-2} (1 mAh cm^{-2}). The ZSN electrode still exhibited stable Zn stripping/plating cycles (Figure 2b). The designed ZSN symmetric cells had a stable cycle life of over 300 h and an overvoltage of only 40 mV, while bare Zn cells presented a cycle life of only 50 h and an overvoltage of up to 150 mV under the same test conditions (Figure 2b). At a high current of 5 mA cm^{-2} (1 mAh cm^{-2}), the prefabricated ZSN symmetric cells still exhibited a highly stable voltage distribution (Figure S9). Even at an ultra-high current density of 10 mA cm^{-2} (10 mAh cm^{-2}), the ZSN symmetrical cells still maintained a stable overvoltage cycle of 150 mV for over 200 h (Figure 2c). The bare Zn battery produced a significant short circuit after only 5 h and an overvoltage of over 600 mV. The unique three-dimensional porous structure of the ZSN electrode provides a channel for the transport of Zn^{2+} , improving the electrical conductivity and ensuring the rapid de-embedding of Zn^{2+} . In addition, the ZSN electrode exhibited a better rate of performance compared to the bare Zn electrode with minimal overpotential at current densities (0.5, 1, 2, 5, 10, and 0.5 mA cm^{-2}) (Figure S10). Then, the cycling performance of the symmetric cells assembled with ZSN and ZS electrodes was compared at a current density of 1 mA cm^{-2} for 1 mAh cm^{-2} (Figure S11). For the first 70 cycles, the ZSN and ZS electrodes exhibited comparable cycling performance, which was attributed to the significant increase of the Sn monomer on the Zn^{2+} nucleation site. In the subsequent cycles, the voltage of the ZS electrode started to fluctuate, which could be attributed to the lack of structural rigidity, causing the Sn layer on the ZS surface to start fracturing and detaching. For symmetric cells assembled with bare Zn and ZSN electrodes, in situ optical microscopy (OM) and electrochemical tests were performed to verify the hydrogen precipitation performance of different electrodes in 2 M ZnSO_4 (Figure 2d,e). On the surface of the bare Zn electrode, at a current density of 5 mA cm^{-2} , small bubbles appeared in the first 20 min while huge bubbles gradually formed after 40 min of reaction and remained attached until 60 min (Figure 2e). The electrode thickness increased significantly, and the surface of the bare Zn metal electrode became loose and severely corroded. On the contrary, for the symmetric cells with the ZSN electrode after the 60 min reaction, the surface of the ZSN electrode remained flat and compact without any bubbles, and the thickness of the electrode remained basically unchanged (Figure 2d). The in situ OM study confirmed that the gas evolution of the ZSN electrode was significantly suppressed during cycling. The ZSN electrode can suppress the side reaction of hydrogen precipitation well due to the interleaved structure of Zn and Sn, the low dielectric constant of the material, and the reduced contact between Zn and the electrolyte. To further evaluate the corrosion resistance of the ZSN samples, Tafel linear polarization tests were performed on ZSN electrodes and bare Zn electrodes. The corrosion current of the ZSN electrode was reduced to 5 mA cm^{-2} compared to the bare Zn electrode, which had a corrosion current of up to 8.1 mA cm^{-2} (Figure 2f), which indicated that the corrosion behavior was suppressed. Polarization resistance (R_p) is also calculated based on the following Stern-Geary formula:

$$R_p = \frac{B_a \times B_c}{2.3(B_a + B_c)} \times \frac{1}{i_{corr}}$$

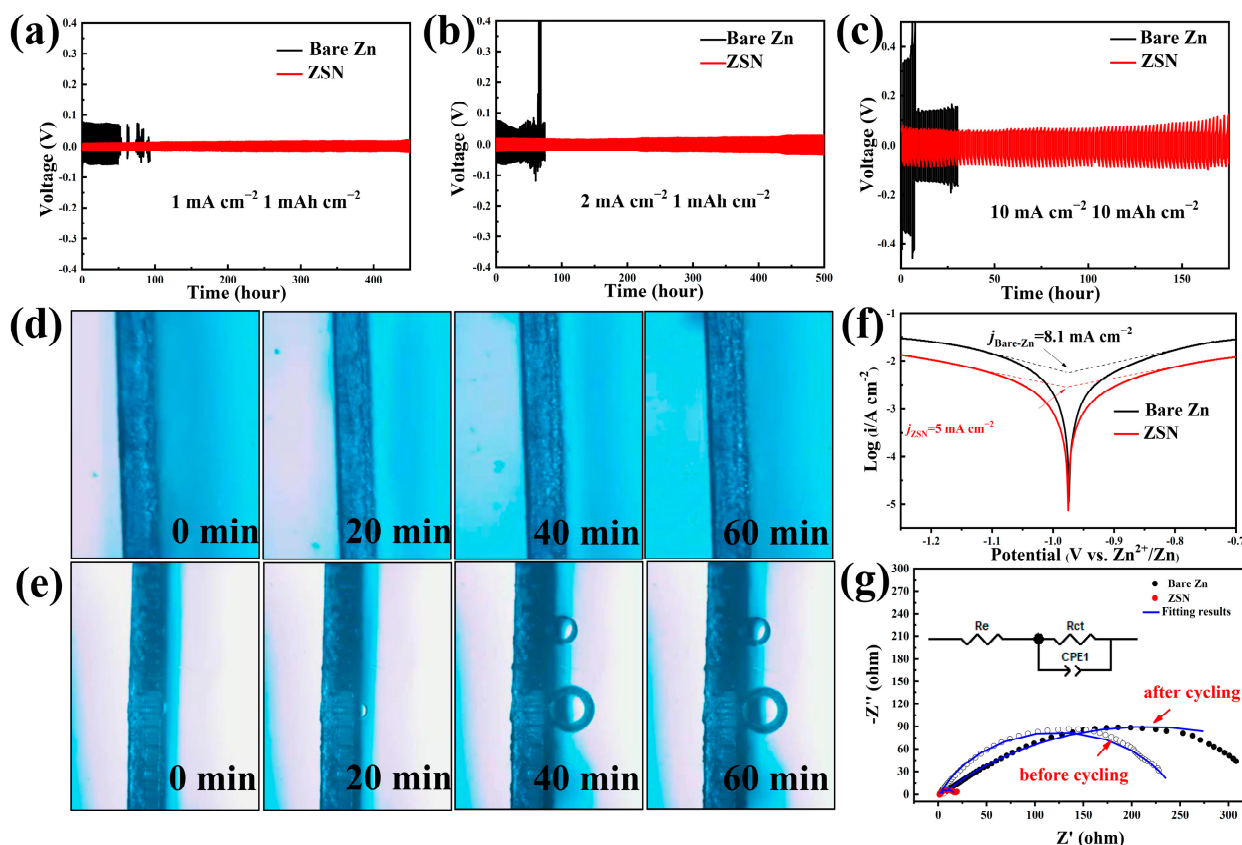


Figure 2. Comparative electrochemical performance test of bare Zn and ZSN symmetric cells. (a–c) Comparison of the cycling performance of bare Zn and ZSN anodes in symmetric cells at 1 mA cm^{-2} and 1 mAh cm^{-2} , 2 mA cm^{-2} and 1 mAh cm^{-2} , and 10 mA cm^{-2} and 10 mAh cm^{-2} , respectively. (d,e) OM images (optical microscope) of (d) the ZSN electrode and (f) the bare Zn electrode stripped at 5 mAh cm^{-2} for one hour. (f) Corrosion curves of bare Zn and ZSN anodes. (g) Impedance spectra of symmetric cells using ZSN and bare Zn electrodes, respectively, before and after 50 cycles.

It has been confirmed that the lower the R_p , the faster the corrosion rate [29,33]. The ZSN anode shows the highest R_p (11.7Ω), while the R_p of the Zn anode is 0.834Ω , suggesting that the ZSN anode can effectively inhibit the corrosion issues. The conductivity of the 3D Sn coating was investigated by impedance testing of the assembled bare Zn and ZSN cells before and after cycling. The electrochemical impedance spectra (EIS) of bare Zn- and ZSN-based ZIBs before and after cycling are shown in Figure 2g and Figure S12. Before cycling, the charge transfer resistance (R_{ct}) of the ZSN symmetric cell (5.5Ω) is much smaller than that of the bare Zn symmetric cell (243.6Ω). After 50 cycles, the impedance changes of the ZSN symmetric cell (varying from the initial 5.5Ω to 16Ω) are much lower than those of the bare Zn symmetric cell (varying from 243.6Ω to 428.7Ω). These results indicate that the introduction of a Sn coating leads to better conductivity and smaller internal resistance, which can greatly reduce the surface hydrogen evolution reaction, volume change, and stripping depth of the electrode.

To verify the wettability of the electrolyte (2 M ZnSO_4) on different electrode surfaces, contact angle tests were performed. It showed that the contact angle between the ZSN electrode and the electrolyte (51.4°) was much smaller than that for bare Zn (93.2° , Figure 3b), which indicated the electrolyte could spread more easily on the ZSN electrode but was much more hydrophilic to the bare Zn electrode. To investigate the effect of ZSN coating on the morphology of Zn deposition, SEM was conducted before cycling and after 50 cycles at 1.0 mA cm^{-2} with a capacity of 1 mA h cm^{-2} in symmetric cells (Figure 3c–h). The surface of bare Zn was relatively smooth and flat. After five cycles, tiny Zn deposits

started to accumulate on the bare Zn surface (Figure 3c), but displayed a large number of prominent Zn dendrites after twenty cycles (Figure 3d), which continued to grow, resulting in many randomly accumulated large lumpy Zn deposits after fifty cycles (Figure 3e). The increased surface area of the bare Zn electrode due to the appearance of Zn dendrites could subsequently puncture the cellulose spacer, resulting in a short circuit or cell failure. Additionally, the cross-sectional SEM image indicated a volume expansion after 50 cycles, with the thickness increasing from the initial 158 μm to 199 μm (Figure S13). On the contrary, the ZSN electrode presented a 3D porous structure on the surface before cycling and almost no change in shape after five cycles (Figure 3f). After 20 plating/peeling cycles, the overall structure and morphology of ZSN electrodes were well maintained (Figure 3g), which proved the excellent mechanical durability and electrochemical cycling of the ZSN electrode in the cell assembly. After 50 cycles, some pores were filled, and the Zn layer was uniform and dense without Zn dendrites or clusters (Figure 3h). This indicates that Zn deposits are preferentially generated in the pores of ZSN, thus avoiding disordered Zn deposition behavior. In addition, the ZSN electrode was thickened by only 9 μm from the initial 200 μm to 220 μm after 50 cycles (Figure S14), which was much smaller than that of the bare Zn electrode and could greatly alleviate the cell volume expansion.

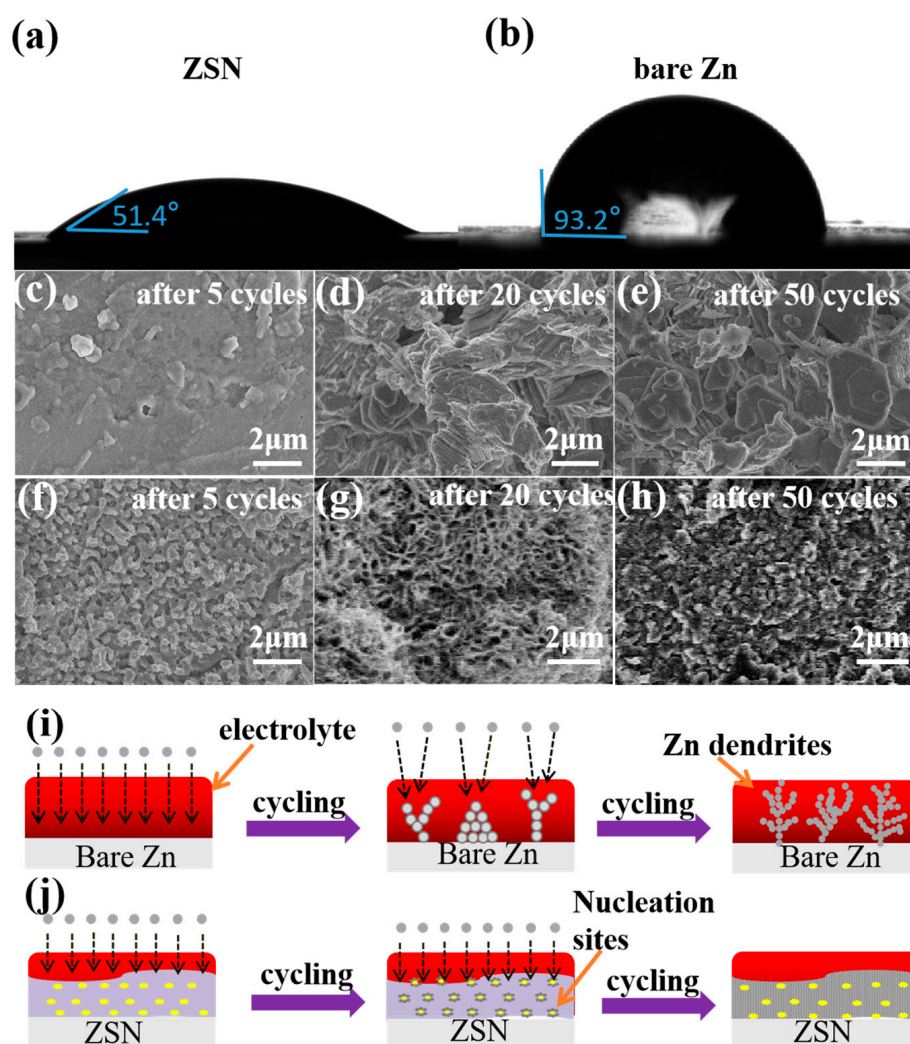


Figure 3. (a,b) Images of the contact angle for the electrolyte with ZSN (a) and bare Zn (b) anodes. (c–h) SEM images of bare Zn and ZSN anodes in symmetric cells after 5, 20, and 50 cycles at 1 ma cm^{-2} , respectively. (i,j) Illustration of the stripping and plating behavior of (i) bare Zn and (j) ZSN electrodes, respectively.

To further investigate the working mechanism of the ZSN electrode, the transport of Zn^{2+} across the bare Zn and ZSN electrodes during the charging and discharging of the battery was simulated. During charging and discharging of bare Zn cells, Zn^{2+} is deposited with favorable energy at charge transfer positions on the anode, with an initial tiny bump formed, on which subsequent Zn^{2+} will be deposited to reduce the surface energy [19]. With a rapid deposition of Zn^{2+} , the nucleation aggregates and the Zn^{2+} concentration increases [19]. The Zn^{2+} in the electrolyte is repeatedly deposited on the anode surface. The inhomogeneous distribution of the electric field and the unrestricted two-dimensional (2D) diffusion of the absorbed Zn^{2+} on the anode surface will lead to the formation of Zn dendrites (Figure 3i). Firstly, when Zn^{2+} is transported in ZSN, the rich interface between the 3D porous Sn and metallic Zn and the high Zn^{2+} conductivity of ZSN ensure rapid diffusion of Zn^{2+} throughout the ZSN composite, which increases the rate capability of the ZSN electrode. In this case, Sn acts as a pro-Zn metal monomer to lower the Zn nucleation potential on ZSN. The introduction of the Sn element increases the hydrogen precipitation energy barrier, inhibits the side reaction of hydrogen precipitation, and provides a uniform surface electric field, inducing uniform Zn deposition behavior and the absence of dendrite diffusion. Secondly, the 3D structure and enhanced mechanical stability of the composite electrode enable the electrode to maintain its structure under high current densities and high fixed surface capacity cycles (Figure 3j). Therefore, the ZSN electrode plays an important role in improving the wettability of the electrode sheet in the electrolyte and regulating the Zn stripping/plating behavior.

As a new type of energy storage device, a hybrid supercapacitor can fully integrate the advantages of batteries and supercapacitors by matching battery-type electrodes and capacitor-type electrodes [40,41]. Zn foil, as the most commonly used anode material for Zn ion supercapacitors in the Zn/Cap configuration, has become a potential safety hazard for electronic devices due to Zn dendrites and corrosion [42]. The ZSN electrode is expected to be an excellent candidate for the Zn foil in the Zn/Cap configuration due to its excellent electrochemical performance exhibited in symmetric cells. To demonstrate the performance advantages of the ZSN electrode in supercapacitors, ZSN hybrid supercapacitors (ZSN||AC) were further assembled with AC as the counter electrode and aqueous ZnSO_4 solution (2 M) as the electrolyte; the schematic diagram is shown in Figure 4a. The stable constant-current charge/discharge curves of ZSN||AC were collected at different current densities from 0.2 to 4 A g^{-1} (Figure 4b). The symmetrical and quasi-triangular-shaped curves indicated a capacitive pseudo-charge storage mechanism. The GCD (galvanostatic charge/discharge) curves maintained symmetry even at a high current density of 4 A g^{-1} and the capacity of the ZSN-based supercapacitor based on the current electrode mass could be maintained at 75 mAh g^{-1} (Figure 4b). The Zn-based supercapacitor was limited by the ion transport capacity of the bare Zn electrode, which hindered charging, and the GCD curves had poor symmetry, which was most evident at low current densities that required long charging and discharging times (Figure 4c).

The energy storage mechanism for this ZSN||AC device is based on Zn plating/stripping at the anode and physical adsorption/desorption of ions at the AC cathode. As shown in Figure 4d, the CV curves of the ZSN||AC device at low rates (such as 1 mV s^{-1}) can exhibit a rectangular shape, reflecting the typical capacitive behavior of this system. Moreover, the CV curves of the ZSN||AC system at higher scan rates (e.g., 20–50 mV s^{-1}) also do not display the severe deformation, implying that the system possesses rapid kinetics during electrochemical reactions and the ability of fast energy storage. The Zn-ion hybrid supercapacitor with ZSN had good cycling stability. During 8000 charge/discharge cycles at 2 A g^{-1} , the supercapacitor always presented a coulombic efficiency close to 100% during cycling and a capacity value of 75 mAh g^{-1} . In contrast, the bare Zn capacitor had a consistently unstable coulombic efficiency during cycling (Figure 4e) and a storage capacity of only 55 mAh g^{-1} . The ZSN anode basically maintained its original morphology after 8000 cycles (Figure S15). The performance comparison

between ZSN||AC and Zn||AC is also at the higher current of 4 A g^{-1} . As shown in Figure S16, the Zn||AC device starts to fail after the 6500th cycle with large fluctuations in capacity and coulombic efficiency. In contrast, ZSN||AC maintains a relatively constant capacity (60 mAh g^{-1}) over 8000 cycles. Regarding the high cycling stability and excellent charge/discharge reversibility of the ZSN||AC, this can be attributed to the low charge transfer resistance of the ZSN electrodes (Figure 4f and Table S2) [43]. Thus, it could provide a higher storage capacity (100 mAh g^{-1}) than that of bare Zn (50 mAh g^{-1}) at a current density of 100 mA g^{-1} (Figure 4g). In addition, ZSN||AC demonstrated good multiplication performance with an average capacity of 80.1 mAh g^{-1} compared to that of Zn||AC (51.89 mAh g^{-1}) at different current densities from 0.2 to 4 A g^{-1} (Figure 4h). In addition, the performance of the ZSN||AC device is better than that of recently reported works about an AC-based system (Table S3).

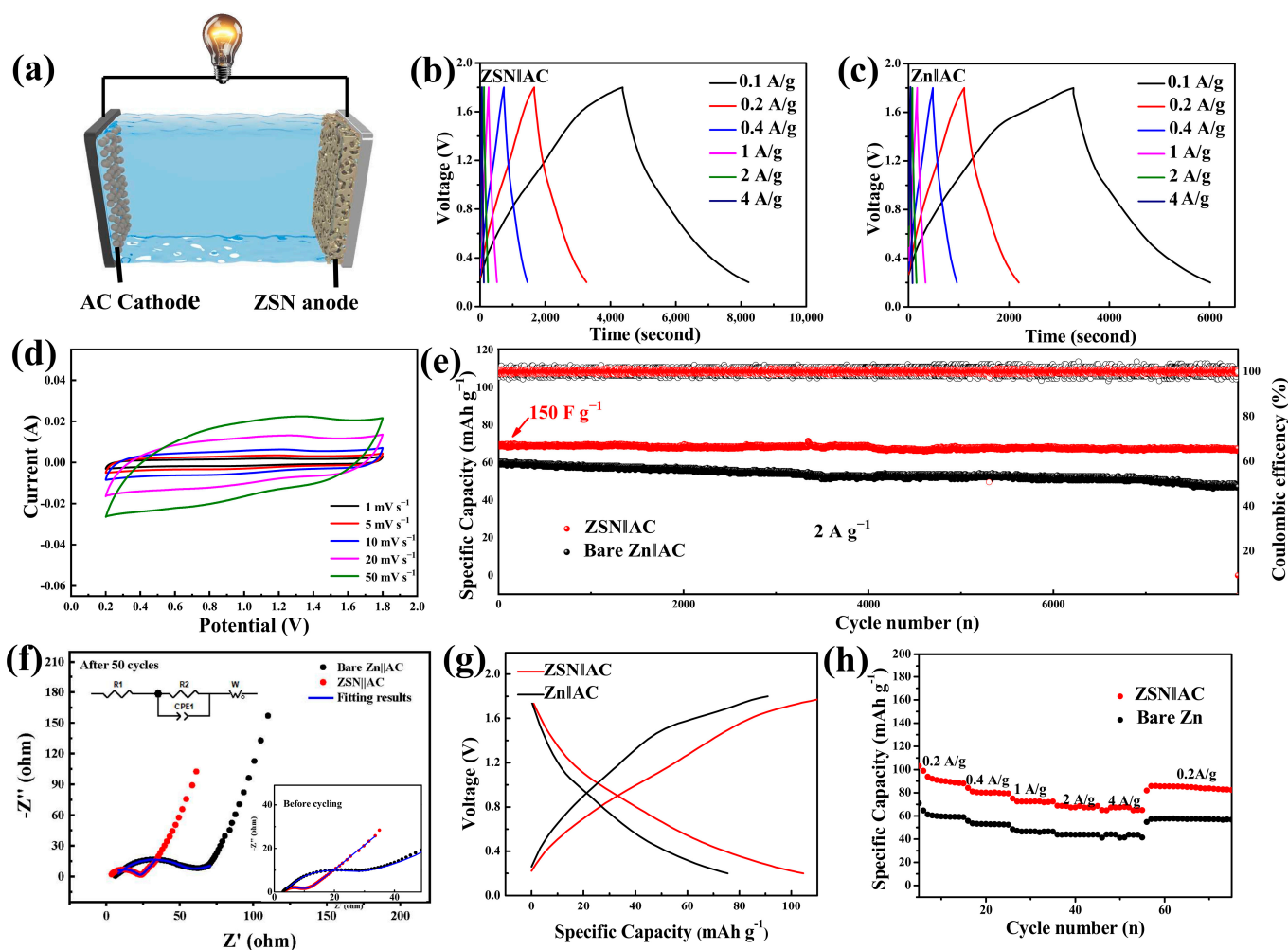


Figure 4. Characterization of electrochemical and cycle performance of zinc-based supercapacitors. (a) Simulation schematic of the ZSN||AC. (b,c) GCD curves of Zn||AC and ZSN||AC at 0.1 A g^{-1} – 4 A g^{-1} . (d) CV curves of ZSN||AC at a scan rate of 1 mV s^{-1} – 50 mV s^{-1} . (e) Long-term cycling capability curves of Zn||AC and ZSN||AC. (f) EIS measurements of Zn||AC and ZSN||AC before and after cycling. (g) Discharge/charge behavior of Zn||AC and ZSN||AC at 0.2 A g^{-1} . (h) Rate performance of Zn||AC and ZSN||AC at a current density from 0.2 A g^{-1} to 4 A g^{-1} .

Manganese-based materials have the merits of low price, environmental friendliness, high discharge voltages, and high specific capacities, which have therefore been widely explored in the field of ZIBs. The Mn^{2+} ions in MnO can be electrochemically oxidized to high valences (+3 or +4) and enable high operating voltages (≈ 1.35 V) [44]. Vanadium-based compounds have an open framework due to their multiple valence oxides and their stable layer structure. Mn^{2+} can be used as a stabilizer or binder to increase the voltage or capacity of pre-intercalated layers of V_2O_5 . Inspired by this, we propose the use of MnV_2O_6 (MVO) as the cathode material for high energy density RAZMBs (rechargeable aqueous Zn metal batteries) to verify the superiority of ZSN anodes. The cycling stability curves and corresponding coulombic efficiency of ZSN||MVO and Zn||MVO cells at a current density of 2 A g^{-1} are shown in Figure 5a. For the Zn||MVO cell, the initial capacity was 180 mA h g^{-1} , which dropped sharply to 60 mA h g^{-1} after 500 cycles, and its coulombic efficiency showed large fluctuations. For the ZSN||MVO cell, less than 5% capacity decay was calculated from cycle 1 to cycle 470, and the coulombic efficiency remained close to 98%. The excellent long-term cycling stability of the ZSN||MVO cells can also be attributed to the excellent electrochemical properties exhibited by the ZSN electrodes, which are perfectly matched to electrode materials requiring metal ion de-embedding. The reversibility of the ZSN anode and the CE cycle stability were also discussed according to its plating/stripping curve (Figure 5b). For the Zn||MVO cell, the bare Zn electrode was still limited by slow Zn^{2+} ion transfer kinetics and the hindered ion migration path would lead to poor reversibility, resulting in the decay of cell capacity. Thus, the charge/discharge curves of the cell exhibited large differences for the 100th and 200th cycles. On the contrary, the plating/stripping curves obtained for the 5th, 100th, and 200th cycles regarding the ZSN||MVO cell were almost superimposed, which further demonstrated the high reversibility of the plating and stripping processes. In addition, the cycling performance at different current densities from 0.5 – 4 A g^{-1} was evaluated (Figure 5c). The ZSN||MVO cell maintained a much higher capacity than that of the Zn||MVO cell at any current density, namely, 0.5 mA h g^{-1} (370 mA h g^{-1} vs. 101 mA h g^{-1}), 1 mA h g^{-1} (310 mA h g^{-1} vs. 70 mA h g^{-1}), 2 mA h g^{-1} (200 mA h g^{-1} vs. 50 mA h g^{-1}), and 4 mA h g^{-1} (150 mA h g^{-1} vs. 35 mA h g^{-1}). Current density returns to 0.5 A g^{-1} after 40 cycles, the average capacity of the ZSN||MVO cell (280 mA h g^{-1}) was significantly higher than that of the Zn||MVO cell (71.4 mA h g^{-1}), which reflected the improved rate and cycling performance of the ZSN anode. The ZSN||MVO device also showed better performance than some of the reported MVO-based systems (Table S4). The ion/electron transfer kinetics of the full cell were analyzed by electrochemical impedance spectroscopy (EIS) analysis (Figure 5d). The charge transfer resistance (R_{ct}) of the ZSN||MVO cell (11.7Ω) was much lower than that of the Zn||MVO cell (130.4Ω). Thus, the excellent performance of the ZSN||MVO cell can be attributed to the high ionic conductivity and the robust ZSN anode. The long cycle stability and the high specific capacity of ZSN||MVO cells make it possible to use them in real electronics. As shown in Figure S17, one ZSN||MVO cell is enough to drive a timer for a long time, and two ZSN||MVO cells in series can keep five LED bulbs on for a long time (Figure 5e).

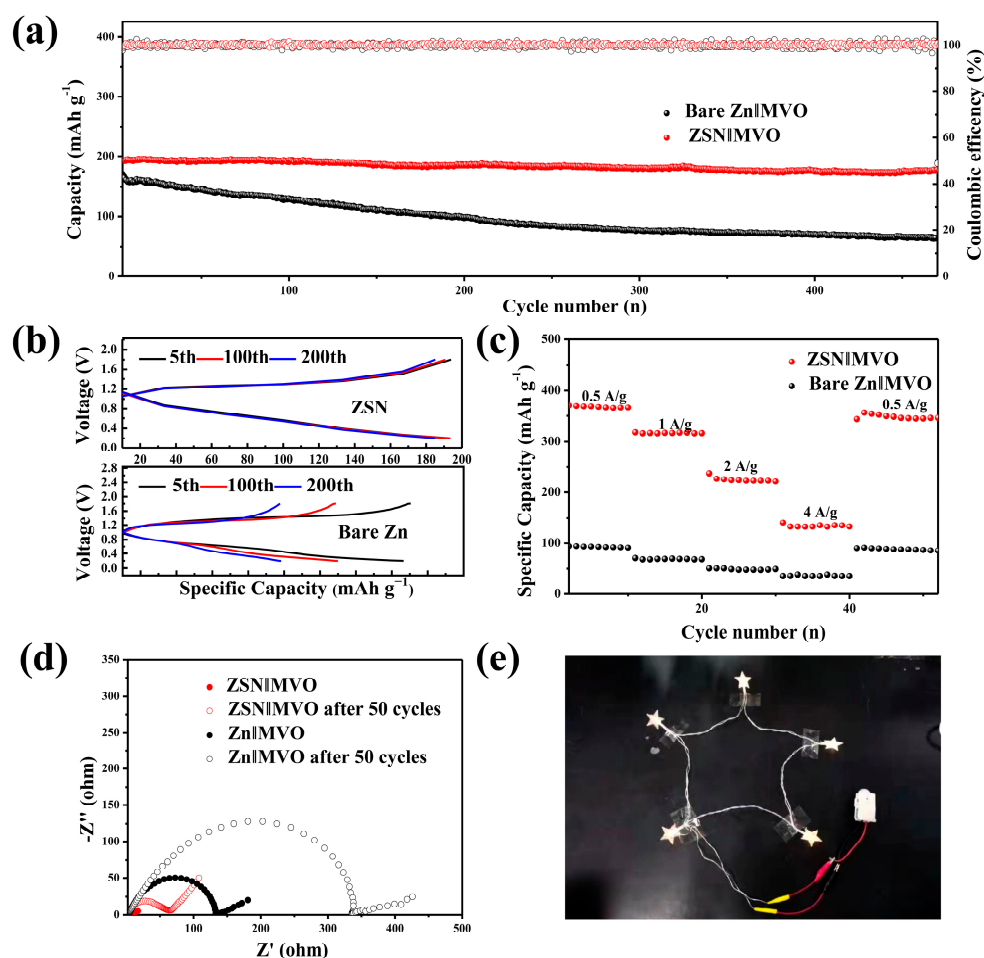


Figure 5. Electrochemical performance testing of Zn-base||MVO cells using ZSN and bare Zn anodes and their practical applications. (a) Cycling performance at a current density of 2 A g^{-1} . (b) Discharge/charge behaviors of Zn||MVO and ZSN||MVO for the 50th, 100th, and 200th cycles. (c) Rate capability of Zn||MVO and ZSN||MVO. (d) EIS plots of Zn||MVO and ZSN||MVO before and after cycling. (e) Application of powering LEDs by two cells connected in series.

4. Conclusions

In this work, an improved substitution reaction provides a very simple way to design 3D porous ZSN structures. ZSN anodes can suppress the volume change of dendrite growth on the electrode surface. The obtained ZSN electrodes can significantly reduce the side reaction of hydrogen precipitation and decrease the volume change of the electrode compared to bare Zn. Meanwhile, the 3D porous ZSN composite structure improves the mechanical stability of the whole electrode and the diffusion behavior of Zn^{2+} ions, resulting in enhanced performance of the ZSN anode in different energy storage elements, especially the deep cycling performance of the Zn metal electrode. The ZSN||ZSN symmetric cell exhibits a highly stable galvanic/stripping behavior over 450 cycles with an overvoltage of 30 mV at 1 mA cm^{-2} and 1 mAh cm^{-2} . In addition, much higher galvanic/peel cycling of the ZSN||ZSN symmetric cell was achieved at deep cycling for high current density and high area capacity (up to 10 mAh cm^{-2} and 10 mAh cm^2). ZSN, as an excellent alternative to bare Zn, exhibits excellent performance in different energy storage devices by matching batteries and supercapacitors. This work opens a new door to the realization of the development of advanced aqueous Zn metal electrodes.

Supplementary Materials: The following supporting information can be downloaded at: <https://www.mdpi.com/article/10.3390/batteries9050262/s1>, Figure S1: Photos of Zn-Li foil under different pressures: (a) 2 MPa; (b) 10 MPa; (c,d) 5 MPa; Figure S2: The thickness of the Zn-Li foil; Figure S3:

SEM/EDS analysis from the (a) cross section and (b) surface of Zn-Li foil; Figure S4: SEM image of the ZS electrode; Figure S5: The Cross-sectional corresponding EDS element mapping(Sn); Figure S6: X-ray diffraction pattern of bare Zn anode; Figure S7: Cycling performance of ZSN anodes prepared with different concentrations of SnCl₄ in symmetric cells at 1 mA cm⁻² for 0.5 mAh cm⁻²; Figure S8: Comparison of the cycling performance of ZL, ZS and ZSN anodes in symmetric cells at 1 mA cm⁻² and 1 mAh cm⁻²; Figure S9: Cycling performance of bare Zn and ZSN anodes at 5 mA cm⁻² and 1 mAh cm⁻²; Figure S10: Rate performance of symmetric cells based on bare Zn and ZSN anodes at current densities from 0.5 to 10 mA cm⁻²; Figure S11: Cycling performance of ZS and ZSN anodes at 1 mA cm⁻² for 1 mAh cm⁻²; Figure S12: Impedance spectra of symmetric cells using ZSN and bare Zn electrodes before and after 50 cycles; Figure S13: Cross-sectional SEM images of the bare Zn electrode (a) before cycling and (b) after 50 cycles at 1.0 mA cm⁻² with a capacity of 1 mA h cm⁻² in a symmetric cell; Figure S14: (a, b) Cross-sectional SEM images of the ZSN electrode after 100 cycles at 1 mA cm⁻² and 1 mAh cm⁻²; Figure S15: SEM and EDS images of the cycled anode in the ZSN||AC system; Figure S16: (a) Long-term cycling capability curves at 4 A g⁻¹ of Zn||AC and ZSN||AC; Figure S17: Photographic image of a normally working electronic chronograph driven by the ZSN||MVO cells; Table S1: Electrochemical performance of Zn stripping/plating of recent reported Zn/Zn symmetrical cells; Table S2: Comparison of the cycling performance of ZSN||AC supercapacitor with some recently reported representative AC capacitors; Table S3: Comparison for the cycling performance of the ZSN||AC supercapacitor with the recently reported AC-based capacitors; Table S4: Cycling performance for the ZSN||MVO battery compared with recently reported batteries using MVO cathodes.

Author Contributions: Conceptualization, D.K.; methodology, D.K. and Z.G.; software, L.L.; formal analysis, D.K., Q.Z. and H.Z.; investigation, D.K.; re-sources, Z.G. and L.W.; data curation, D.K. and Q.Z.; writing—original draft preparation, D.K.; writing—review and editing, L.L., H.Z., R.L. and Z.G.; visualization, L.L.; supervision, Z.G. and L.W.; project administration, Z.G.; funding acquisition, H.Z., Z.G. and L.W. All authors have read and agreed to the published version of the manuscript.

Funding: The authors acknowledge funding support from the National Natural Science Foundation of China (51772162), the Youth Innovation and Technology Foundation of Shandong Higher Education Institutions, China (2019KJC004), the Outstanding Youth Foundation of Shandong Province, China (ZR2019JQ14), the Taishan Scholar Young Talent Program, the Major Scientific and Technological Innovation Project (2019JZZY020405), the Postdoctoral Science Foundation of China (2019M652499), and the Postdoctoral Innovation Project of Shandong Province (201903021). Application for independent research and innovation projects of graduate students of Qingdao University of Science and Technology (B2022KY009).

Data Availability Statement: Data available on request from the authors.

Conflicts of Interest: The authors declare no conflict of interest.

References

1. Xiao, R.; Cai, Z.; Zhan, R.; Wang, J.; Ou, Y.; Yuan, Z.; Wang, L.; Lu, Z.; Sun, Y. Localizing concentrated electrolyte in pore geometry for highly reversible aqueous Zn metal batteries. *Chem. Eng. J.* **2021**, *420*, 129642. [[CrossRef](#)]
2. Liao, M.; Ji, X.; Cao, Y.; Xu, J.; Qiu, X.; Xie, Y.; Wang, F.; Wang, C.; Xia, Y. Solvent-free protic liquid enabling batteries operation at an ultra-wide temperature range. *Nat. Commun.* **2022**, *13*, 6064. [[CrossRef](#)] [[PubMed](#)]
3. Xie, Y.; Huang, J.; Kong, T.; Zhou, X.; Wu, K.; Liu, X.; Yi, J.; Xing, L.; Xia, Y. Moisture-activated deep eutectic electrolyte enabling stable metal Zn anode. *Energy Storage Mater.* **2023**, *56*, 218–226. [[CrossRef](#)]
4. Guo, Z.; Wang, F.; Xia, Y.; Li, J.; Tamirat, A.G.; Liu, Y.; Wang, L.; Wang, Y.; Xia, Y. In situ encapsulation of core-shell-structured Co@Co₃O₄ into nitrogen-doped carbon polyhedra as a bifunctional catalyst for rechargeable Zn-air batteries. *J. Mater. Chem. A* **2020**, *8*, 19057. [[CrossRef](#)]
5. Xie, C.; Li, Y.; Wang, Q.; Sun, D.; Tang, Y.; Wang, H. Issues and solutions toward zinc anode in aqueous zinc-ion batteries: A mini review. *Carbon Energy* **2020**, *2*, 540–560. [[CrossRef](#)]
6. Yan, L.; Zeng, X.; Li, Z.; Meng, X.; Wei, D.; Liu, T.; Ling, M.; Lin, Z.; Liang, C. An innovation: Dendrite free quinone paired with ZnMn₂O₄ for zinc ion storage. *Mater. Today Energy* **2019**, *13*, 323–330. [[CrossRef](#)]
7. Tang, B.; Shan, L.; Liang, S.; Zhou, J. Issues and opportunities facing aqueous zinc-ion batteries. *Energy Environ. Sci.* **2019**, *12*, 3288–3304. [[CrossRef](#)]
8. Yi, Z.; Chen, G.; Hou, F.; Wang, L.; Liang, J. Strategies for the Stabilization of Zn Metal Anodes for Zn-Ion Batteries. *Adv. Energy Mater.* **2021**, *11*, 2003065. [[CrossRef](#)]

9. Gao, X.; Zhang, H.; Liu, X.; Lu, X. Flexible Zn-ion batteries based on manganese oxides: Progress and prospect. *Carbon Energy* **2020**, *2*, 387–407. [[CrossRef](#)]
10. Shangguan, E.; Wang, L.; Wang, Y.; Li, L.; Chen, M.; Qi, J.; Wu, C.; Wang, M.; Li, Q.; Gao, S.; et al. Recycling of Zinc–Carbon Batteries into MnO/ZnO/C to Fabricate Sustainable Cathodes for Rechargeable Zinc-Ion Batteries. *ChemSusChem* **2022**, *15*, e202200720. [[CrossRef](#)] [[PubMed](#)]
11. Zheng, J.; Zhan, C.; Zhang, K.; Fu, W.; Nie, Q.; Zhang, M.; Shen, Z. Rapid Electrochemical Activation of V₂O₃@C Cathode for High-Performance Zinc-Ion Batteries in Water-in-Salt Electrolyte. *ChemSusChem* **2022**, *15*, e202200075. [[CrossRef](#)] [[PubMed](#)]
12. Shen, Z.; Tang, Z.; Li, C.; Luo, L.; Pu, J.; Wen, Z.; Liu, Y.; Ji, Y.; Xie, J.; Wang, L.; et al. Precise Proton Redistribution for Two-Electron Redox in Aqueous Zinc/Manganese Dioxide Batteries. *Adv. Energy Mater.* **2021**, *11*, 2102055. [[CrossRef](#)]
13. He, H.; Qin, H.; Wu, J.; Chen, X.; Huang, R.; Shen, F.; Wu, Z.; Chen, G.; Yin, S.; Liu, J. Engineering interfacial layers to enable Zn metal anodes for aqueous zinc-ion batteries. *Energy Storage Mater.* **2021**, *43*, 317–336. [[CrossRef](#)]
14. Huang, J.; Chi, X.; Du, Y.; Qiu, Q.; Liu, Y. Ultrastable Zinc Anodes Enabled by Anti-Dehydration Ionic Liquid Polymer Electrolyte for Aqueous Zn Batteries. *ACS Appl. Mater. Interfaces* **2021**, *13*, 4008–4016. [[CrossRef](#)]
15. Zhang, C.; Shin, W.; Zhu, L.; Chen, C.; Neuefeind, J.C.; Xu, Y.; Allec, S.I.; Liu, C.; Wei, Z.; Daniyar, A.; et al. The electrolyte comprising more robust water and superhalides transforms Zn-metal anode reversibly and dendrite-free. *Carbon Energy* **2020**, *3*, 339–348. [[CrossRef](#)]
16. Cao, J.; Zhang, D.; Gu, C.; Wang, X.; Wang, S.; Zhang, X.; Qin, J.; Wu, Z. Manipulating Crystallographic Orientation of Zinc Deposition for Dendrite-free Zinc Ion Batteries. *Adv. Energy Mater.* **2021**, *11*, 2101299. [[CrossRef](#)]
17. Shin, J.; Lee, J.; Kim, Y.; Park, Y.; Kim, M.; Choi, J.W. Highly Reversible, Grain-Directed Zinc Deposition in Aqueous Zinc Ion Batteries. *Adv. Energy Mater.* **2021**, *11*, 2100676. [[CrossRef](#)]
18. Yan, H.; Li, S.; Nan, Y.; Yang, S.; Li, B. Ultrafast Zinc–Ion–Conductor Interface toward High-Rate and Stable Zinc Metal Batteries. *Adv. Energy Mater.* **2021**, *11*, 2100186. [[CrossRef](#)]
19. Li, B.; Zhang, X.; Wang, T.; He, Z.; Lu, B.; Liang, S.; Zhou, J. Interfacial Engineering Strategy for High-Performance Zn Metal Anodes. *Nano-Micro Lett.* **2021**, *14*, 6. [[CrossRef](#)]
20. Guo, Z.; Fan, L.; Zhao, C.; Chen, A.; Liu, N.; Zhang, Y.; Zhang, N. A Dynamic and Self-Adapting Interface Coating for Stable Zn-Metal Anodes. *Adv. Mater.* **2021**, *34*, 2105133. [[CrossRef](#)]
21. Li, C.; Shi, X.; Liang, S.; Ma, X.; Han, M.; Wu, X.; Zhou, J. Spatially homogeneous copper foam as surface dendrite-free host for zinc metal anode. *Chem. Eng. J.* **2020**, *379*, 122248. [[CrossRef](#)]
22. Zhang, Q.; Luan, J.; Fu, L.; Wu, S.; Tang, Y.; Ji, X.; Wang, H.-Y. The Three-Dimensional Dendrite-Free Zinc Anode on a Copper Mesh with a Zinc-Oriented Polyacrylamide Electrolyte Additive. *Angew. Chem. Int. Ed.* **2019**, *58*, 15841–15847. [[CrossRef](#)]
23. Liu, X.; Yang, F.; Xu, W.; Zeng, Y.; He, J.; Lu, X. Zeolitic Imidazolate Frameworks as Zn²⁺ Modulation Layers to Enable Dendrite-Free Zn Anodes. *Adv. Sci.* **2020**, *7*, 2002173. [[CrossRef](#)]
24. Zeng, Y.; Zhang, X.; Qin, R.; Liu, X.; Fang, P.; Zheng, D.; Tong, Y.; Lu, X. Dendrite-Free Zinc Deposition Induced by Multifunctional CNT Frameworks for Stable Flexible Zn-Ion Batteries. *Adv. Mater.* **2019**, *31*, 1903675. [[CrossRef](#)]
25. Chen, T.; Wang, Y.; Yang, Y.; Huang, F.; Zhu, M.; Ang, B.T.W.; Xue, J.M. Heterometallic Seed-Mediated Zinc Deposition on Inkjet Printed Silver Nanoparticles Toward Foldable and Heat-Resistant Zinc Batteries. *Adv. Funct. Mater.* **2021**, *31*, 2101607. [[CrossRef](#)]
26. Xia, A.; Pu, X.; Tao, Y.; Liu, H.; Wang, Y. Graphene oxide spontaneous reduction and self-assembly on the zinc metal surface enabling a dendrite-free anode for long-life zinc rechargeable aqueous batteries. *Appl. Surf. Sci.* **2019**, *481*, 852–859. [[CrossRef](#)]
27. Kumar, D.; Ail, U.; Wu, Z.; Björk, E.M.; Berggren, M.; Gueskine, V.; Crispin, X.; Khan, Z. Zinc salt in “Water-in-Polymer Salt Electrolyte” for Zinc-Lignin Batteries: Electroactivity of the Lignin Cathode. *Adv. Sustain. Syst.* **2022**, *7*, 2200433. [[CrossRef](#)]
28. Yan, M.; Xu, C.; Sun, Y.; Pan, H.; Li, H. Manipulating Zn anode reactions through salt anion involving hydrogen bonding network in aqueous electrolytes with PEO additive. *Nano Energy* **2021**, *82*, 105739. [[CrossRef](#)]
29. Guo, W.; Zhang, Y.; Tong, X.; Wang, X.; Zhang, L.; Xia, X.; Tu, J. Multifunctional tin layer enabled long-life and stable anode for aqueous zinc-ion batteries. *Mater. Today Energy* **2021**, *20*, 100675. [[CrossRef](#)]
30. Zhang, S.; Hao, J.; Luo, D.; Zhang, P.; Zhang, B.; Davey, K.; Lin, Z.; Qiao, S. Dual-Function Electrolyte Additive for Highly Reversible Zn Anode. *Adv. Energy Mater.* **2021**, *11*, 2102010. [[CrossRef](#)]
31. Yang, X.; Li, C.; Sun, Z.; Yang, S.; Shi, Z.; Huang, R.; Liu, B.; Li, S.; Wu, Y.; Wang, M.; et al. Interfacial Manipulation via In Situ Grown ZnSe Cultivator toward Highly Reversible Zn Metal Anodes. *Adv. Mater.* **2021**, *33*, 2105951. [[CrossRef](#)]
32. Liu, J.; Song, W.; Wang, Y.; Wang, S.; Zhang, T.; Cao, Y.; Zhang, S.; Xu, C.; Shi, Y.; Niu, J.; et al. A polyamino acid with zincophilic chains enabling high-performance Zn anodes. *J. Mater. Chem. A* **2022**, *10*, 20779–20786. [[CrossRef](#)]
33. Yan, J.; Ye, M.; Zhang, Y.; Tang, Y.; Li, C.C. Layered zirconium phosphate-based artificial solid electrolyte interface with zinc ion channels towards dendrite-free Zn metal anodes. *Chem. Eng. J.* **2022**, *432*, 134227. [[CrossRef](#)]
34. Lu, X.; Zhao, C.; Chen, A.; Guo, Z.; Liu, N.; Fan, L.; Sun, J.; Zhang, N. Reducing Zn-ion concentration gradient by SO₄²⁻-immobilized interface coating for dendrite-free Zn anode. *Chem. Eng. J.* **2023**, *451*, 138772. [[CrossRef](#)]
35. Cai, Z.; Ou, Y.; Zhang, B.; Wang, J.; Fu, L.; Wan, M.; Li, G.; Wang, W.; Wang, L.; Jiang, J.; et al. A Replacement Reaction Enabled Interdigitated Metal/Solid Electrolyte Architecture for Battery Cycling at 20 mA cm⁻² and 20 mAh cm⁻². *J. Am. Chem. Soc.* **2021**, *143*, 3143–3152. [[CrossRef](#)]
36. Fan, X.; Yang, H.; Wang, X.; Han, J.; Wu, Y.; Gou, L.; Li, D.; Ding, Y. Enabling Stable Zn Anode via a Facile Alloying Strategy and 3D Foam Structure. *Adv. Mater. Interfaces* **2021**, *8*, 2002184. [[CrossRef](#)]

37. Kim, Y.-J.; Ryu, K.-S. The surface-modified effects of Zn anode with CuO in Zn-air batteries. *Appl. Surf. Sci.* **2019**, *480*, 912–922. [[CrossRef](#)]
38. Du, Y.; Liu, C.; Liu, Y.; Han, Q.; Chi, X.; Liu, Y. Carbon fiber micron film guided uniform plating/stripping of metals: A universal approach for highly stable metal batteries. *Electrochim. Acta* **2020**, *339*, 135867. [[CrossRef](#)]
39. Wang, A.; Zhou, W.; Huang, A.; Chen, M.; Chen, J.; Tian, Q.; Xu, J. Modifying the Zn anode with carbon black coating and nanofibrillated cellulose binder: A strategy to realize dendrite-free Zn-MnO₂ batteries. *J. Colloid Interface Sci.* **2020**, *577*, 256–264. [[CrossRef](#)] [[PubMed](#)]
40. Zhou, X.; Dai, H.; Huang, X.; Ren, Y.; Wang, Q.; Wang, W.; Huang, W. Porous trimetallic fluoride Ni-Co-M (M = Mn, Fe, Cu, Zn) nanoprisms as electrodes for asymmetric supercapacitors. *Mater. Today Energy* **2020**, *17*, 100429. [[CrossRef](#)]
41. Xu, T.; Wang, D.; Li, Z.; Chen, Z.; Zhang, J.; Hu, T.; Zhang, X.; Shen, L. Electrochemical Proton Storage: From Fundamental Understanding to Materials to Devices. *Nano-Micro Lett.* **2022**, *14*, 126. [[CrossRef](#)]
42. Dunn, B.; Kamath, H.; Tarascon, J.-M. Electrical Energy Storage for the Grid: A Battery of Choices. *Science* **2011**, *334*, 928–935. [[CrossRef](#)] [[PubMed](#)]
43. Allagui, A.; Baboukani, A.R.; Elwakil, A.S.; Wang, C. Electrochemical stability analysis of red phosphorus-based anode for lithium-ion batteries. *Electrochim. Acta* **2021**, *395*, 139149. [[CrossRef](#)]
44. Li, P.; Ren, J.; Li, C.; Li, J.; Zhang, K.; Wu, T.; Li, B.; Wang, L. MOF-derived defect-rich CeO₂ as ion-selective smart artificial SEI for dendrite-free Zn-ion battery. *Chem. Eng. J.* **2023**, *451*, 138769. [[CrossRef](#)]

Disclaimer/Publisher’s Note: The statements, opinions and data contained in all publications are solely those of the individual author(s) and contributor(s) and not of MDPI and/or the editor(s). MDPI and/or the editor(s) disclaim responsibility for any injury to people or property resulting from any ideas, methods, instructions or products referred to in the content.